JACS
JOURNAL OF THE AMERICAN CHEMICAL SOCIETY
pubs.acs.org/JACS
Article

Dynamic Transformation of High-Architectural Nanocrystal Superlattices upon Solvent Molecule Exposure

Yasutaka Nagaoka, Jeremy Schneider, Na Jin, Tong Cai, Yuzi Liu, Zhongwu Wang, Ruipeng Li, Kyung-Suk Kim, and Ou Chen*

Cite This: J. Am. Chem. Soc. 2024, 146, 13093−13104
Read Online
ACCESS | Metrics & More | Article Recommendations | Supporting Information

ABSTRACT: The cluster-based body-centered-cubic superlattice (cBCC SL) represents one of the most complicated structures among reported nanocrystal assemblies, comprised of 72 truncated tetrahedral quantum dots per unit cell. Our previous report revealed that truncated tetrahedral quantum dots within cBCC SLs possessed highly controlled translational and orientational order owing to an unusual energetic landscape based on the balancing of entropic and enthalpic contributions during the assembly process. However, the cBCC SL's structural transformability and mechanical properties, uniquely originating from such complicated nanostructures, have yet to be investigated. Herein, we report that cBCC SLs can undergo dynamic transformation to face-centered-cubic SLs in response to post-assembly molecular exposure. We monitored the dynamic transformation process using in situ synchrotron-based small-angle X-ray scattering, revealing a dynamic transformation involving multiple steps underpinned by interactions between incoming molecules and TTQDs' surface ligands. Furthermore, our mechanistic study demonstrated that the precise configuration of TTQDs' ligand molecules in cBCC SLs was key to their high structural transformability and unique jelly-like soft mechanical properties. While ligand molecular configurations in nanocrystal SLs are often considered minor features, our findings emphasize their significance in controlling weak van der Waals interactions between nanocrystals within assembled SLs, leading to previously unremarked superstructural transformability and unique mechanical properties. Our findings promote a facile route toward further creation of soft materials, nanorobotics, and out-of-equilibrium assemblies based on nanocrystal building blocks.

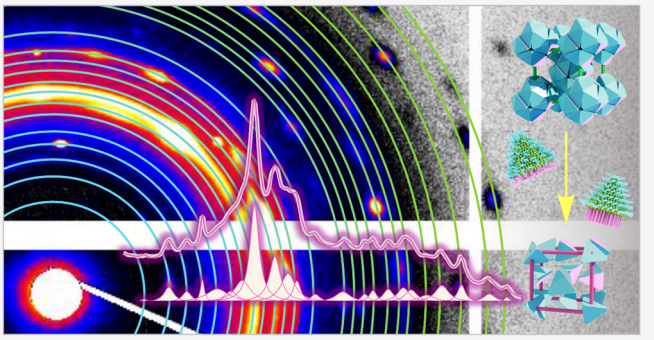

Downloaded via BROWN UNIV on May 23, 2024 at 13:17:54 (UTC).
See https://pubs.acs.org/sharingguidelines for options on how to legitimately share published articles.

1. INTRODUCTION

Dynamic materials capable of active three-dimensional (3D) transformations have garnered significant interest due to their capability for realizing life-inspired organizations.[1−4] These materials hold great promise for applications in biomedicine,[1,4] flexible electronics,[5,6] soft robotics,[7−12] and nanomachines.[9,10] In the laboratory, researchers have employed liquid crystals,[13−15] gels,[11,12,16] soft polymers,[11,12] and supramolecular materials[17,18] to ensure mechanical and chemical flexibility, which can enable system interactions with the surrounding environment. In these systems, soft noncovalent intermolecular interactions, such as ion-dipole, dipole−dipole, hydrogen bonding, and $\pi-\pi$ interactions, play a crucial role in constructing materials' structures and rendering flexible mechanical properties to these materials.[16,19−22] These relatively weak forces also impart the sensitivity to respond to molecular triggering systems.[11,13,16,19−22] By harnessing energy from external stimuli and/or their surroundings, these triggering systems induce mechanical and physical movements in the dynamic 3D nanostructures.[11,17] In several triggering systems reported so far, molecular recognition stands as one of the most essential mechanisms among various chemical and biological systems, enabling critical functionalities.[11,23] The development of effective transformation systems necessitates comprehensive design strategies that consider and leverage these underlying mechanisms.[3] Through the utilization of soft noncovalent interactions and molecular recognition, the full potential of dynamic 3D nanoarchitectures can be unlocked, leading to innovative and functional materials with diverse applications.[3]

Transformable nanocrystal superlattices (NC-SLs) hold great promise due to the exceptional properties of NC building blocks and their desirable structural characteristics.[24−33] However, research in this area has been limited; conventional NC-SLs primarily rely on strong van der Waals

Received: December 22, 2023
Revised: April 16, 2024
Accepted: April 18, 2024
Published: May 1, 2024

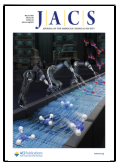

ACS Publications
© 2024 American Chemical Society

https://doi.org/10.1021/jacs.3c14603
J. Am. Chem. Soc. 2024, 146, 13093−13104

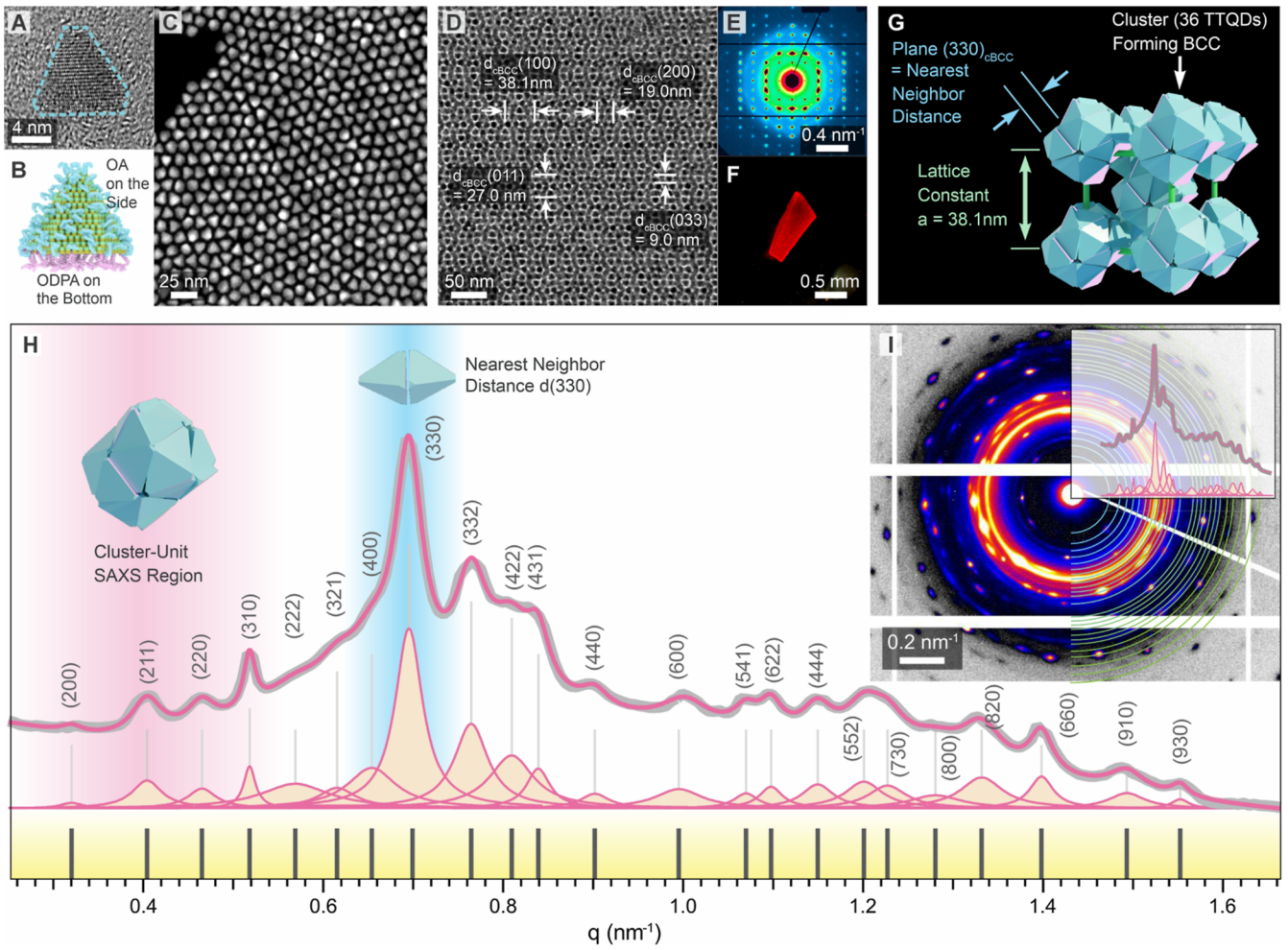

Figure 1. Characterizations of truncated tetrahedral quantum dot (TTQD) NC building blocks and cBCC NC-SLs. (A) High-resolution (HR)-transmission electron microscopy (TEM) image showing an individual TTQD. (B) Corresponding atomic model of the TTQD. (C) High-angle annular dark-field imaging (HAADF)-TEM visualization of TTQDs. (D) TEM image of a cBCC NC-SL viewed via $[110]_{cBCC}$ projection, and (E) Corresponding SAXS pattern for the cBCC NC-SL. (F) Photograph displaying a piece of the cBCC supercrystal. (G) Computer model of a cBCC NC-SL unit cell. (H) Integrated 1D SAXS pattern of the cBCC NC-SL powder sample represented with a gray line, with fitted patterns and constituent peaks indicated in pink. The pink and blue shaded areas are the SAXS peak areas for cluster-based structures and nearest neighbor distance, respectively. (I) Corresponding 2D SAXS pattern of the cBCC NC-SL powder sample.

(vdW) interactions between NCs for structural integrity,[21,34−36] making them unresponsive to external stimuli. A recent work demonstrated dynamically transformable NC-SLs achieved by tethering NCs with tecton ligands through hydrogen bonding.[24] The authors demonstrated that the NC-SLs could alter their superstructures when the solvent was switched from toluene to *n*-decane, which affected ligand molecules' configuration.[24] Moreover, to gain insight into the dynamic process from the NC superstructure scale down to the molecular level, detailed time-resolved in situ measurements become vital. Recent advancements in in situ techniques for NC self-assemblies have revealed unprecedented molecular movement and dynamics at the (sub)nanometer scale, which can provide valuable information about underlying mechanisms during NC self-assembly processes.[37−39]

In this study, we present a comprehensive investigation of dynamic NC-SLs in response to molecule exposure, utilizing time-resolved in situ synchrotron-based small-angle X-ray scattering (SAXS) measurements. We found that cluster-based body-centered cubic (cBCC) SLs formed from truncated-tetrahedral quantum dots (TTQDs) exhibit delicate and weak inter-TTQD vdW interactions due to the unique coiled molecular configurations within their ligand surfactants. As a result, the cBCC SL solids exhibit jelly-like soft mechanical properties with a dynamic transformability to face-centered cubic (FCC) upon exposure to specific solvents or vapor infusion into the lattices. We show that fine molecular configuration and recognition play critical roles in determining interparticle interactions and superstructural transformations within the NC-SLs, an aspect that was largely overlooked prior to this work. Our findings offer valuable insights into the design and understanding of transformable NC-SL solids, marking an important advancement in exploring and harnessing dynamic NC-superstructured materials and their potential applications in various fields such as biomimetics, flexible electronics, and soft robotics.

2. RESULTS

Wurtzite (WZ) CdSe−CdS core−shell QDs with a truncated-tetrahedral shape (denoted as TTQDs) were synthesized using our previously reported method.[40,41] Figure 1A−C shows a high-resolution TEM image, a corresponding computer model,

https://doi.org/10.1021/jacs.3c14603
J. Am. Chem. Soc. 2024, 146, 13093−13104

and a low-magnification scanning TEM (STEM) image of the TTQD building blocks, respectively. The TTQDs possess an inorganic height of 8.2 ± 0.4 nm along the $(0002)_{WZ}$ direction and a base edge length of 10.8 ± 0.6 nm (bottom $(0002)_{WZ}$ facet) with 2.4 nm truncation (see also Figures S1−S3 in the Supporting Information for detailed shape information). Notably, TTQDs retain an anisotropic surface ligand coverage:[40−42] the bottom base (i.e., $(0002)_{WZ}$ facet) is covered by octadecylphosphonic acid (ODPA), and all the equivalent sides (i.e., $\{10\bar{1}1\}_{WZ}$ facets) are tethered with oleic acid (OA) (Figure 1B). Subsequently, cBCC NC-SLs were fabricated by slowly evaporating hexane in a TTQD solution (~20 mg/mL),[40] as confirmed by low-magnification TEM images showing a characteristic wavy pattern with designated lattice fringes, as shown in Figure 1D (27.0 nm spacing between two adjacent strong fringe lines. See also Figure S4). A 2D synchrotron-based SAXS pattern of a submillimeter-sized 3D single supercrystal further validated the distinctive high-architectural cBCC superstructure, displaying a single-crystal-line-type spotted pattern with an orthogonal-based symmetry viewed from the [110] projection of a BCC lattice (Figures 1E,F, S5, and Table S1).[40] The wide-angle X-ray scattering (WAXS) pattern showcased the same atomic orientational ordering as we previously observed (Figure S5).[40] A lattice parameter (a_{cBCC}) of 38.1 ± 0.4 nm was then determined (Figure 1E, and Table S1), consistent with the simulated computer model of the cBCC unit cell (Figure 1G). The SAXS pattern of the cBCC SL powders and the corresponding integrated 1D SAXS plot further confirmed the cBCC SL structure (Figures 1H, I; S6, S7; and Table S2). The most intense SAXS peak is positioned at a q-value of 0.700 nm^{-1} (Table S2), which has been assigned to the $d(330)_{cBCC}$ scattering feature of the cBCC structure (indicated by blue shading in Figure 1H). Additionally, a unique set of scattering peaks in the low-q region of 0.3−0.5 nm^{-1} arises from the cBCC cluster subunit comprising 36 TTQDs (highlighted by pink shading in Figure 1H).[40]

To test the solvent-induced structural transformation, we subjected the cBCC SL powder sample to immersion in 12 different solvents with a constant duration time of 20 s (see SI for details). Three distinctive structural outcomes, i.e., cBCC, FCC, and amorphous (Figure 2), were obtained after the solvent immersion experiments with the summarized results provided in Table 1 (also see Table S3). Notably, immersion of the cBCC SL powders in EG, diethylene glycol (DEG), dimethyl sulfoxide (DMSO), or water did not disrupt the pristine cBCC SL structure, as evidenced by an unchanged lattice parameter of 38.1 nm (Figure 2 and Table 1). This structural preservation was consistently observed even when extending the immersion time to 24 h, yielding no measurable changes in the superstructure (Figure S8). In contrast, when immersing the same cBCC SL powder sample in nonpolar solvents, i.e., toluene, chloroform, or hexane, the resulting 1D SAXS pattern only showed three broad scattering features in the q-value range of 0.6 to 2.5 nm^{-1} (Figure 2). This SAXS pattern matched well to the pattern simulated solely on the basis of particle form factors with an effective size of 10.2 nm (Figure 2 and Table 1), suggesting a superstructure solvation process. With prolonged immersion time, complete dissolution of the SL sample was observed, in good accordance with the high colloidal dispersibility of TTQDs in these applied nonpolar solvents.[41] The most intriguing result was obtained by immersing the sample in a series of solvents, including

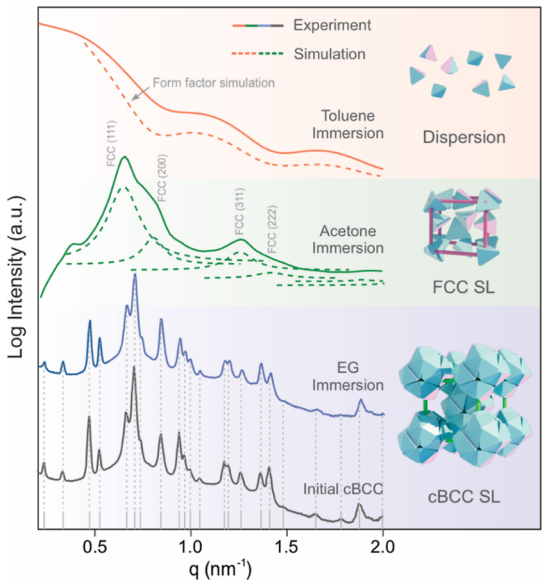

Figure 2. SAXS patterns before and after solvent exposure. SAXS pattern of cBCC NC-SLs before solvent exposure (bottom), SAXS pattern after ethylene-glycol (EG) immersion (second from bottom), after acetone immersion (second from top), and after toluene immersion (top). Adjacent to each SAXS pattern, a computational model is presented representing the resulting superstructures. Dotted lines in the top and second tops illustrate the simulation spectra for the assigned structures.

ethanol, methanol, ethyl acetate, acetone, and isopropanol. This led to a superstructural phase transition from the initial cBCC structure to a final FCC SL configuration (Figure 2, and Table 1). Notably, a significantly reduced lattice parameter was observed for the obtained FCC SLs, ranging from 13.6 to 15.4 nm (as compared to 38.1 nm of the starting cBCC SLs) (Table 1, S9, S10 and Tables S4−S8). Although the influence of solvents on NC-SL formation has been widely examined in previous studies,[34,40,42,43] postformation SL transformations in response to solvent exposure are rarely explored to our best knowledge.[24,26]

To closely monitor the TTQD NC-SL phase transformations in response to the solvent molecules, we conducted TTQD NC-SL vapor-exposure experiments using a specially designed vapor chamber setup (Scheme 1). In these experiments, the SL structural evolution was continuously monitored through time-resolved in situ SAXS measurements (further details are provided in Supporting Information). The vapor chamber was configured with a reservoir containing the applied solvent (i.e., acetone or toluene), creating a controlled environment saturated with solvent vapor. The cBCC SL powder sample was positioned on one inner side of the chamber window, which was then irradiated by synchrotron X-ray irradiation for SAXS measurements (Scheme 1). SAXS patterns for the acetone (toluene) vapor-exposure experiment were recorded for more than 20 h (10 h) at a constant time interval of 65 s (11 s). This setup allowed us to investigate the SL transformation process in situ with sufficient time resolution to capture the intricate SL transition dynamics triggered by vaporized solvent molecules.

The in situ SAXS measurements conducted in the acetone vapor chamber (with a vapor pressure of 30.8 KPa) showed that the same cBCC-to-FCC SL phase transformation occurred, as observed in the acetone solvent-immersion

https://doi.org/10.1021/jacs.3c14603
J. Am. Chem. Soc. 2024, 146, 13093−13104

Table 1. Solvent Parameters and Results of Solvent Immersion Experiments

	resulting SL	resulting LC[a]	vol./one NC (nm^3)	interfacial energy[b] (mN m^{-1})	δP polar	Ra[b] (HSP[a])	density (g/cm^3)
water	cBCC	38.1 (±0.4) nm	768.2	**55.77**	16.0	45.3	1
EG[a]	cBCC	38.1 (±0.4) nm	768.2	**27.19**	11.0	28.3	1.115
DEG[a]	cBCC	38.1 (±0.4) nm	768.2	**23.19**	2.9	6.6	1.120
DMSO[a]	cBCC	38.1 (±0.4) nm	768.2	**21.39**	16.4	19.7	1.092
methanol	FCC	15.4 ± 0.5 nm	913.1	**10.03**	12.3	25.7	0.791
isopropanol	FCC	15.3 ± 0.6 nm	895.4	**5.97**	6.1	17.5	0.785
ethanol	FCC	14.9 ± 0.6 nm	827.0	**2.15**	8.8	21.3	0.789
EA[a]	FCC	14.5 ± 0.6 nm	762.2	**4.60**	5.3	9.0	0.895
acetone	FCC	13.6 ± 0.4 nm	628.9	**5.82**	10.4	12.7	0.785
toluene	dissolve	N/A	N/A	**1.73**	1.4	4.0	0.867
chloroform	dissolve	N/A	N/A	**−5.30**	0.0	3.0	1.479
hexane	dissolve	N/A	N/A	**0.80**	3.1	7.1	0.659

[a]Abbreviations used in this table: EG: ethylene glycol, DEG: diethylene glycol, DMSO: dimethyl sulfoxide, EA: ethyl acetate, LC: lattice constant, and HSP: Hansen solubility parameter. [b]The calculated interfacial energies and the HSP values are for referred solvent molecules and hydrocarbon-chain parts of surfactant molecules, i.e., OA and ODPA. See details in the Supporting Information. The complete set of data is presented in Table S3 in the Supporting Information.

Scheme 1. Schematic Illustration of In Situ SAXS Measurements for Solvent-Vapor-Exposure Experiments. (A) Vapor Chamber Used for In Situ SAXS Measurements. (B) Illustration of NC-SL Transformation From cBCC to FCC Superstructure Occurred During the Solvent-Vapor−Exposure Experiments

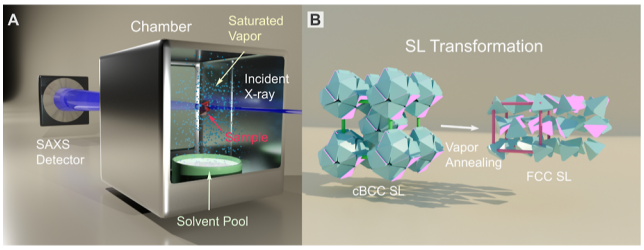

experiment, however, with a much slower SL transformation rate (Figure 3A). Monitoring the entire transition process over a course of approximately 21 h (~76000 s) unveiled a smooth and gradual evolution of the SL structure (Figure 3A and Movies S1, S2). To elucidate the structural evolution, we plotted the position and intensity of the strongest scattering peak (i.e., $d(330)_{cBCC}$ and $d(111)_{FCC}$), along with the calculated effective volume per TTQD NC as a function of the vapor-exposure time (Figure 3B−E). Notably, five distinct transition stages, denoted as stages a1−a5 (color-coded in Figure 3A), were identified during the course of SL transformation, as detailed below (Figure 3A−E).

In stage a1 (0 s−ca. 260 s), all the SAXS peaks continuously shifted toward lower q-values (e.g., $d(330)_{cBCC}$ shifted from 0.710 to 0.692 nm^{-1}) with increased peak intensities (Figures 3B−S11, and Tables S9, S10). This suggested a uniform lattice expansion while maintaining the initial cBCC SL structure. The unit-cell volume expanded from 5.57×10^4 nm^3 to 6.01×10^4 nm^3 at an expansion rate of 17.1 nm^3/s (equivalent to 238 Å^3/NC s and a volume expansion rate of 3.07×10^{-2}%/s, see Supporting Information for calculation details) (Figure 3D). This volume expansion was likely due to the inclusion of vaporized acetone molecules into the SLs (thus inducing configuration changes of the NC surface ligands; see Discussion Section for details), with a molecular inclusion rate of 1.3 acetone/NC s (Figure 3D). In stage a2 (ca. 260 s−2600 s), the cBCC SL continued expanding, yet at a significantly reduced rate (unit-cell volume expansion rate of 0.22 nm^3/s, 3.1 Å^3/NC s, and 3.66×10^{-4}%/s) compared to that in stage a1 (Figures 3D, S12, and Table S11). The equivalent molecular inclusion rate dropped sharply to 0.015 acetone/NC s (Figure 3D). By the end of stage a2, the unit-cell volume of the cBCC SL had expanded from 5.57×10^4 nm^3 to 6.06×10^4 nm^3 (Figure 3D), corresponding to an 8.8% volume expansion relative to the pristine structure.

Transitioning to stage a3 (ca. 2600 − 30,000 s), the cBCC SL structure started degrading, indicated by the broadening and diminished intensity of all the SAXS peaks (Figures 3A,C,E−H and S12). A new shoulder peak emerged at a slightly larger q-value of ~0.720 nm^{-1} next to the primary $d(330)_{cBCC}$ scattering peak (Figures 3F, and S12), indicating elevated and nonuniform local strain originating from the $(330)_{cBCC}$ crystal planes.[44] Progressing to stage a4 from around 30,000 s to approximately 69,000 s, the sample exhibited a decline in the SAXS fine features, accompanied by continuously decreasing peak intensities (Figures 3C,G,H, S13, and Table S11). In addition, gradual vanishing of the characteristic cBCC cluster subunit scattering peaks (within the low-q region of 0.3−0.6 nm^{-1}) unambiguously revealed a superstructure reconstruction of the initial cBCC SL (Figures 3G and S13). Finally, around 69,000 s (starting of stage a5), the cBCC SL fully transited to an FCC structure with a unit-cell lattice parameter of 14.5 ± 0.4 nm, which remained nearly unchanged for ~6000 s before stopping the SAXS pattern collection (Figures 3C, S13, and Table S10). Such drastic lattice parameter contraction (from 38.2 nm for the initial cBCC SL to 14.5 nm for final FCC SL) indicated that the final FCC SL structure was constructed from individual TTQDs with the absence of any higher-order building units, in line with the loss of the cluster-based subunits indicated by the in situ SAXS data (Scheme 1 and Figure 3A,G). Intriguingly, both the initial cBCC SL and the final FCC SL showed similar TTQD NC densities (i.e., 774 nm^3/NC vs 740−785 nm^3/NC, Figure 3E). This finding suggests that comparable effective volumes per TTQD were attained for both superstructures (i.e., cBCC vs FCC) at two different equilibrium states despite distinct assembly fashions of the TTQD NCs.

Next, we conducted another vapor-exposure experiment using a toluene solvent pool (vapor pressure of 3.76 kPa) over a span of ~10 h (~35,000 s) and collected in situ SAXS

https://doi.org/10.1021/jacs.3c14603
J. Am. Chem. Soc. 2024, 146, 13093−13104

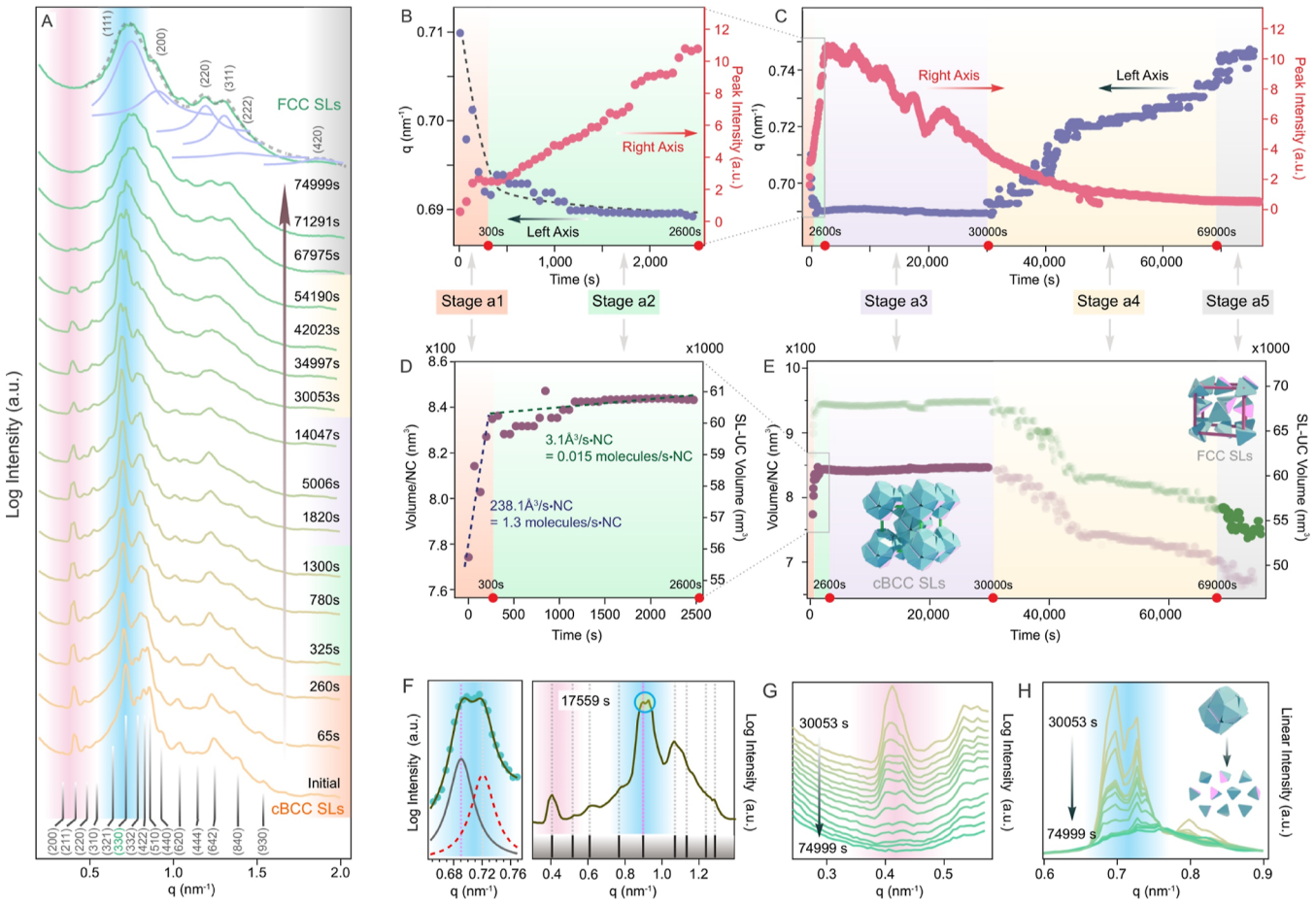

Figure 3. In situ SAXS measurement results during the acetone−vapor−exposure experiment. (A) Series of representative in situ SAXS patterns obtained during the acetone−vapor−exposure experiment. The five identified distinct stages are color-coded: stage a1 (orange), stage a2 (green), stage a3 (purple), stage a4 (yellow), and stage a5 (gray). (B,C) Plots over acetone−vapor−exposure time vs. peak position (left axis) and peak intensity (right axis) for the most intense peak in the SAXS patterns, i.e., $d(330)_{cBCC}$ for cBCC NC-SLs and $d(111)_{FCC}$ for FCC NC-SLs: zoom-in stages a1, a2 (B) and stages a1−a5 (C). (D,E) Plots over acetone−vapor−exposure time vs. volume per NC in the SL (left axis) and SL unit cell (SL-UC) volume (right axis) for zoom-in stage a1, a2 (D) and stage a1−a5 (E). Purple and green marks represent calculated values based on the cBCC and FCC SL structures, respectively. The solid circles represent the values calculated based on our structure assignments, i.e., cBCC structure for stages a1−a3, and FCC structure for stage a5, while semitransparent circles represent calculated values based on the SL structures that were not assigned as such. Please note that the structure in stage a4 is transient, and neither cBCC nor FCC can be assigned during the course of stage a4. (F) SAXS pattern at 17,559 s: zoom-in $(330)_{cBCC}$ peak region showing the main peak (black line) and an emergent shoulder peak (dotted red line) (left panel); the corresponding zoom-out SAXS pattern (right panel). (G,H) SAXS patterns during stages a4 and a5 for the range denoting the cluster-based subunits (0.25−0.55 nm^{-1}) (G), and main $d(330)_{cBCC}$ peak area (0.6−0.9 nm^{-1}) (H).

patterns to monitor the structural evolution (Figure 4, and Movies S3, S4). The final SAXS pattern clearly demonstrated the complete dissolution of the initial cBCC SL structure (Figure 4A,J), aligning with the result of the toluene-immersion experiment (Figure 2). A thorough analysis of the SAXS results from the toluene−vapor−exposure experiment revealed five distinguishable SL transition stages, denoted as stages t1-t5 (color-coded in Figure 4A). Analogous to the acetone−vapor−exposure experiment, stage t1 and t2 showed the preservation of the pristine cBCC SL, yet with different expansion rates of unit-cell volume: 6.48×10^{-2}%/s ≈ 508 $Å^3$/NC s in stage t1 (0 s−ca. 300 s) and 2.58×10^{-3}%/s ≈ 24.1 $Å^3$/NC s in stage t2 (ca. 300 s−6000 s) (Figure S14, Tables S12−S14). These volume expansion rates were about 2−7 fold of the expansion rates measured from the acetone−vapor−exposure experiment (stage a1, a2), manifesting a faster intake of solvent molecules (4.1 toluene/NC s and 0.20 toluene/NC·s for stage t1 and t2, respectively), while minimal ligand configuration change should happen under this condition.[20,34]

By the end of stage t2, the cBCC unit-cell volume increased from 5.64×10^4 nm^3 to 7.73×10^4 nm^3 (equivalent to 290 nm^3/NC, Table S14) (Figure 4D), representing a 37.1% volume expansion, notably larger than that in the acetone vapor experiment (i.e., 9.2%). These accelerated solvent-molecule-intake rates and the substantial unit-cell volume expansion can be attributed to the higher molecular affinity between toluene and the TTQD surface ligand molecules (i.e., OA and ODPA) compared to acetone, originated from their similar molecular properties (see Tables 1 and S2). Meanwhile, the SAXS peak intensities showed an initial increase until around 3000 s, followed by a subsequent decrease in stage t2 (Figure 4C). This trend suggested that the structural integrity of the cBCC SL started to deteriorate with expanding the cBCC unit-cell volume. This observation was further supported by the shift and eventual disappearance of the SAXS peaks in the low-q region, as illustrated in Figure 4E. This is in striking contrast to the result from the acetone−vapor−exposure experiment (Figure 3), in accordance with the

https://doi.org/10.1021/jacs.3c14603
J. Am. Chem. Soc. 2024, 146, 13093−13104

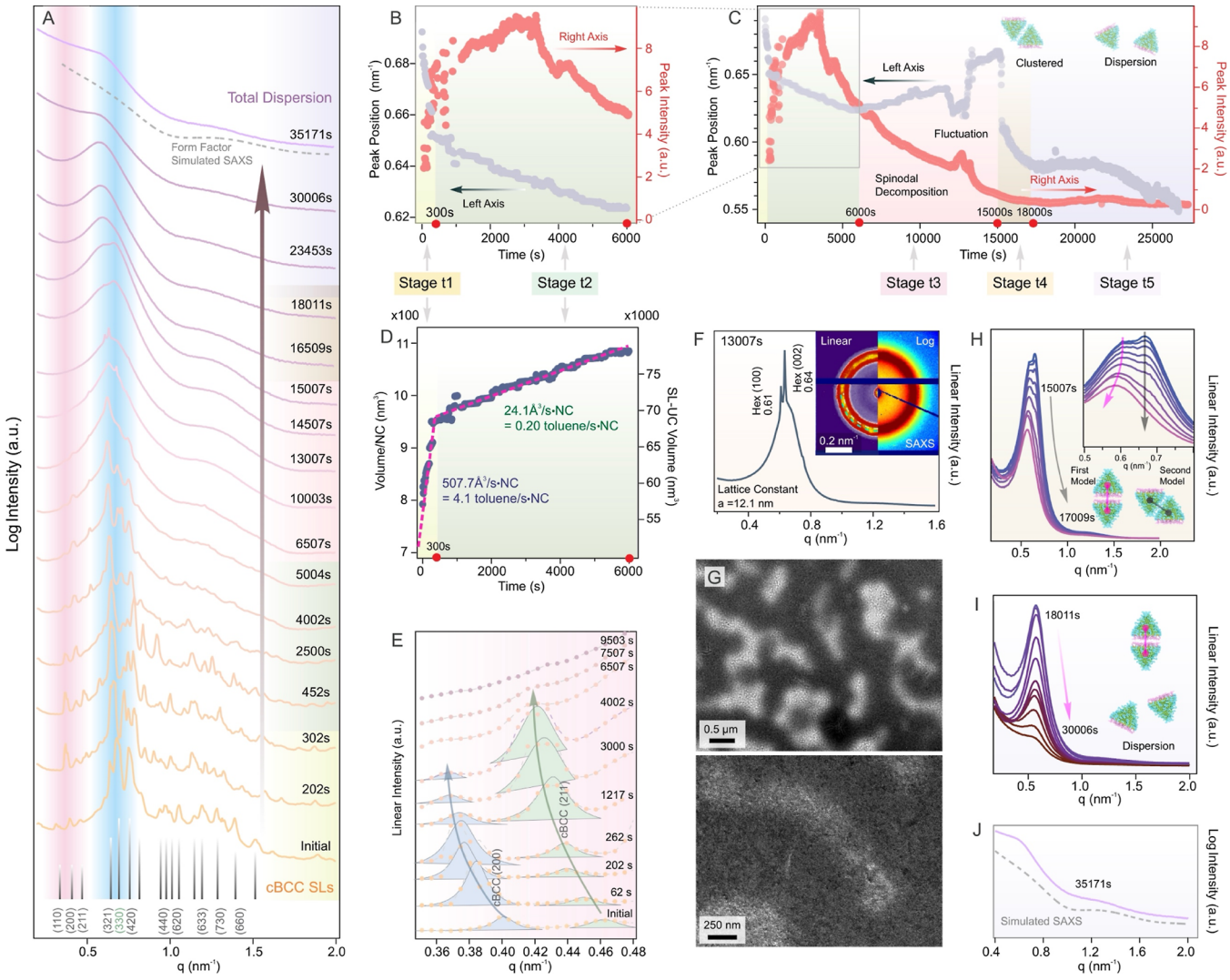

Figure 4. In situ SAXS measurement results during toluene−vapor−exposure experiment. (A) Series of representative in situ SAXS patterns obtained during the toluene-vapor-exposure experiment. The five identified distinct stages are color-coded: stage t1 (yellow), stage t2 (green), stage t3 (pink), stage t4 (brown), and stage t5 (purple). (B,C) Plots over toluene-vapor-exposure time vs. peak position (left axis) and peak intensity (right axis) for the most intense peak in the SAXS patterns, i.e., $d(330)_{cBCC}$ for cBCC NC-SLs and $d(111)_{FCC}$ for FCC NC-SLs: zoom-in stages t1−t2 (B) and stages t1−t5 (C). (D) Plots over toluene vapor exposure time vs. volume per NC in the SL (left axis) and SL unit cell (SL-UC) volume (right axis) during stage t1−t2. (E) Evolution of the SAXS patterns in the low-q region responsible for cluster-based subunits during stage t1−t3. (F) SAXS pattern at 13,007 s (in stage t3), displaying peaks corresponding to hexagonal (100) and hexagonal (002) peaks of the spinodal decomposition structures. inset: the corresponding 2D SAXS pattern with different intensity scales: linear (left) and log scale (right). (G) TEM images with different magnifications of TTQD NCs under supersaturation conditions show a spinodal decomposition-like pattern. (H) SAXS pattern evolution in stage t4. Inset: zoomed-in SAXS pattern evolution for the major peaks representing the two-types of TTQD-dimers with either $\{0002\}_{WZ}$-to-$\{0002\}_{WZ}$ (pink) or $\{10\bar{1}1\}_{WZ}$-to-$\{10\bar{1}1\}_{WZ}$ (black) alignments. (I) SAXS pattern evolution during stage t5. (J) Final SAXS pattern at 35171 s, with a simulated pattern (dotted line) based on the TTQD NC form factor, indicating complete NC dissolution in toluene.

varied intermolecular interactions between the TTQD ligands and different solvent molecules.

In stage t3, from ca. 6000 to 15,000 s, the SAXS patterns exhibited peculiar changes attributed to macroscopic spinodal decomposition. Within this stage, the characteristic cBCC cluster subunit features in the low-q region gradually disappeared, along with continuously declining peak intensities across all other SAXS features (Figures 4A and S15). Interestingly, we observed a consistent redshift of the SAXS peaks to larger q-values (smaller d-spacings), coincident with a fluctuation in peak position and intensity of the strongest SAXS feature (Figure 4C). A closer look at the SAXS patterns within this period (i.e., ca. 12,000 − 13,200 s) revealed that the fluctuation was induced by a sporadic emergence of intense spotted signals observed in 2D SAXS patterns (Figures 4F and S15). The positions of these newly emerged peaks were consistent with a hexagonal-based SL structure with a lattice parameter of 12.1 nm (Figure S15 and Table S15). Such spinodal decomposition structures generally arise when the dispersant concentration surpasses the dispersibility limit in a specific solvent (under the supersaturation condition).[45−47] The corresponding TEM images confirmed the spinodal decomposition by showing a characteristic dendritic pattern with irregular microstructures of ∼100−500 nm (Figures 4G and S16). The generation of the spinodal structures well explained the observed SAXS-peak redshifts (d-spacing reduction), as shorter average interparticle distances should be expected under a supersaturation (superdispersion)

https://doi.org/10.1021/jacs.3c14603
J. Am. Chem. Soc. 2024, 146, 13093−13104

Scheme 2. Schematic Illustration of the Dynamic Transformation Process From the cBCC NC-SLs to FCC NC-SLs. (A) Computational Models of OA, ODPA, and TTQD NCs Passivated With These Ligands in Two Distinct Solvent Environments: Non-Polar (on the Left) and Polar (on the Right). (B) Illustrations of Two Molecular Configurations of the Ligands Between Adjacent TTQD NCs: (i) Coiled Molecular Configuration Exhibiting Soft Touches Between Adjacent TTQD NCs Leading to Weak vdW Interactions; (ii) Straight Configuration With Enhanced Ligand-Interdigitations Between Adjacent TTQD NCs. The Molecular Touching Areas Were Highlighted With Red in the Illustration. (C) Proposed Mechanism for the Observed Stepwise Superstructural Transformations During the Two Types of Vapor-Exposure Experiments Using Different Solvents: Acetone (Top) and Toluene (Bottom)

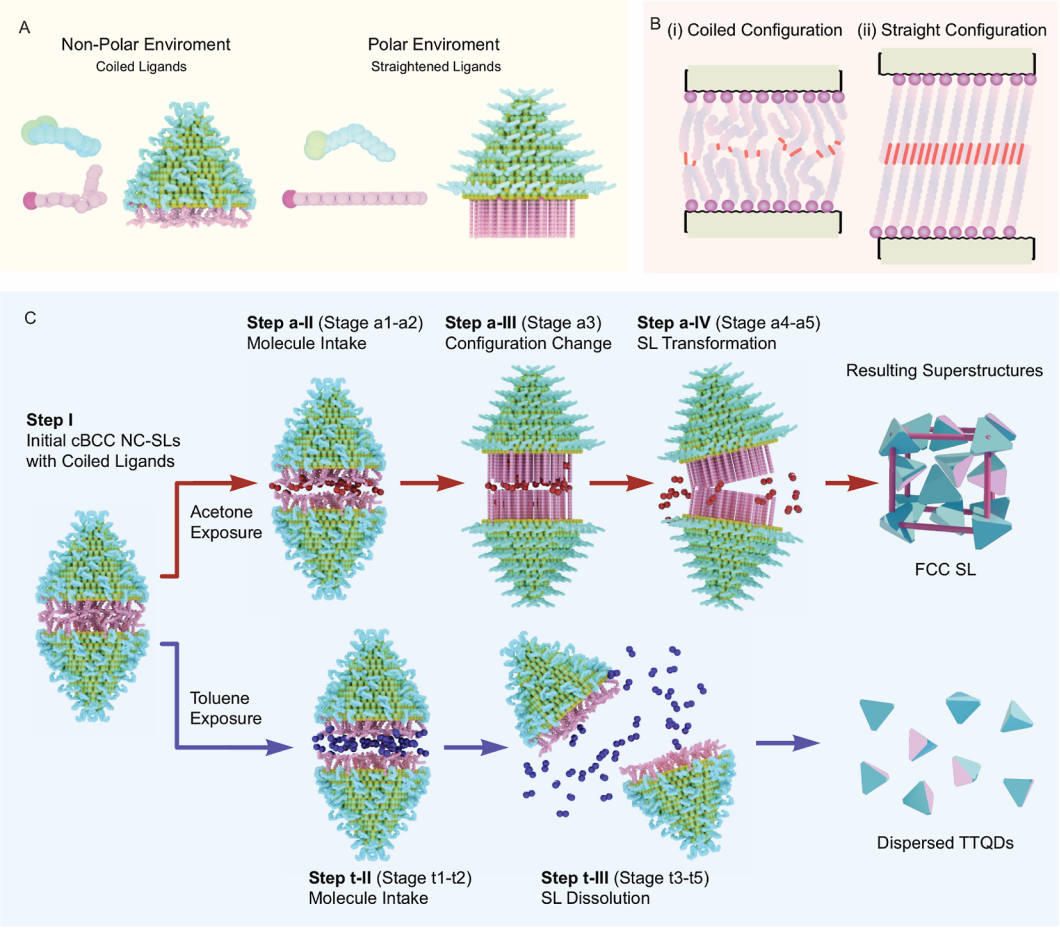

condition (Figure 4C,G).[45−47] By the end of stage t3 (~15,000 s), the SAXS profile in the main scattering region (~0.6−0.7 nm^{-1}) displayed a dual-peak feature at 0.616 and 0.667 nm^{-1}, corresponding to the *d*-spacings of 10.2 and 9.42 nm, respectively (Figures 4H and S17). These *d*-spacings aligned well with the two different inter-TTQD distances of local TTQD-dimer configurations (the smallest building unit of the cBCC SL structure[40]): 10.2 nm for the TTQD-dimers with bottom $\{0002\}_{WZ}$-to-$\{0002\}_{WZ}$ alignment; 9.42 nm for the TTQD-dimers with side $\{10\bar{1}1\}_{WZ}$-to-$\{10\bar{1}1\}_{WZ}$ alignment (Figures 4H,I, and S17).[40,42] This result demonstrated that the basic and smallest structural configuration (i.e., TTQD-dimer units) remained by the end of stage t3 despite the dissolution of the overall cBCC superstructure.

In stage t4, from ca. 15,000 to 18,000 s, the spinodal structure began collapsing, evident from drastic blueshifts and continuous declining intensities across all the remaining SAXS peaks (Figures 4A,H and S18). Concurrently, during this stage, the dual-peak scattering feature in the main scattering region gradually disappeared (Figure 4H). Specifically, the larger *q*-value peak at 0.667 nm^{-1} (smaller *d*-spacing of 9.42 nm) gradually vanished, while the smaller *q*-value peak at 0.616 nm^{-1} (larger *d*-spacing of 10.2 nm) continuously blue-shifted to an even smaller *q*-value of 0.581 nm^{-1} (enlarged *d*-spacing of 10.8 nm) (Figure 4H). This anisotropic peak evolution behavior indicated that the TTQD-dimers oriented with the bottom $\{0002\}_{WZ}$-to-$\{0002\}_{WZ}$ alignment persisted for a longer period of time (survived through stage t4) during the toluene-vapor-induced superstructure dissolution process. Likely, the greater stability of facet registration resulted from the stronger molecular interactions among ODPA ligands on the bottom $\{0002\}_{WZ}$ facets of the TTQD NCs in comparison to those of OA ligands on the side $\{10\bar{1}1\}_{WZ}$ facets.[40,42] In the final stage t5 (ca. 18,000−35,000 s), SAXS patterns gradually lost all the scattering features from short-range orderings (Figure 4H−I). At 35,171 s, the final SAXS spectrum solely exhibited the signals from the form factor of the TTQD NCs without any periodic lattices (Figures 4J and S19), consistent with the result obtained from the toluene-immersion experiment, signifying the complete dispersion of TTQD NCs (Figure 2).

https://doi.org/10.1021/jacs.3c14603
J. Am. Chem. Soc. 2024, 146, 13093−13104

3. DISCUSSION

To gain a deeper understanding of the solvent-induced postformation NC-SL transformation, we investigated four solvent-specific parameters: solvent polarity, Hansen solubility parameter, hydrostatic pressure, and solvent−ligand interfacial energy (Tables 1 and S3). While solvent polarity and the Hansen-solubility factor are commonly used to elucidate colloidal dispersibility,[48−50] neither parameter showed a consistent trend that could explain the final transformed superstructural results we observed (Tables 1 and S3). External pressure has been considered a potential stimulus for inducing superstructural transformations,[51−54] yet the calculated hydrostatic pressure generated by the solvent immersion remained low, falling within the pressure range of 6−15 Pa (see calculation details in Supporting Information). This pressure range is about 8−9 orders of magnitude lower than the typical pressure (1−10 GPa) required to induce any form of SL change.[51−57] Finally, our investigation indicated that the interfacial energy between the surfactant and the incoming solvent molecules, i.e., wettability,[20,58,59] potentially played a pivotal role in driving the observed SL phase transformation (see Method and Table S3 in the Supporting Information). The cBCC-to-FCC superstructural transformation occurred exclusively when the solvent−ligand interfacial energy was in the range of 2.2−10.2 mN/m (Table 1). In contrast, the cBCC SL structure remained intact when the interfacial energy exceeded 21 mN/m. This result suggests that effective molecular interactions between the TTQD ligands and incoming solvent molecules are the key to triggering the superstructural transformations in the adaptable cBCC NC-SLs.

Our analysis verifies that the cBCC SLs can actively interact with specific incoming molecules, thereby inducing changes in the microenvironment, e.g., polarity, around NCs' surfactants. Consequently, the molecular configuration of the ligands alters depending on the surrounding microenvironment, ultimately leading to a multistage transformation in the NC superstructure at a macroscopic level. We propose that the transformation of TTQD SLs from a cBCC to an FCC structure is dictated by alternations in the configuration of surfactant molecules upon intaking exposed solvent molecules, as illustrated in Scheme 2.[60−64] First, the formation of TTQD NC-SLs with a cBCC structure requires the use of zero-polarity solvents like hexane or cyclohexane, in which the ligand molecules (i.e., OA and ODPA) adopt a highly coiled molecular configuration due to solvation effects (Scheme 2A).[60,61,64,65] These highly coiled ligands inhibit effective intercalations or partial crystallization among the hydrocarbon chains of ligand molecules on the surfaces of adjacent aligned TTQD NCs (Scheme 2B).[20] Instead, weak vdW bonds form at random points of contact among coiled ligand molecules (Scheme 2Bi), in line with previous studies on the friction between molecular layers with coiled or rigid molecular configurations.[20,66] As a result, the cBCC SL structure is held by delicate and labile interligand interactions, as evidenced by its soft and jelly-like property (Figure S20).[66] Even under gentle pressure (mashing process, approximately 100−500 kPa, see Method and Figure S20 in the Supporting Information), the cBCC SLs can transform into a short-range ordered FCC structure with a lattice constant of 16.2 ± 0.7 nm (Figure S21 and Table S16). This stands in contrast to conventional NC-SL materials, which typically maintain their initial superstructure even when subjected to external pressures as high as 5−10 GPa.[51−57] This notably low SL phase transition pressure (100−500 kPa) suggests that cBCC NC-SLs is a metastable structure that underscores the exceptionally weak bond rupture forces of 4.6−23 pN among the surface ligands of neighboring TTQD NCs within the cBCC SLs (see Method S1 for calculation details), lower than the typical vdW bond strength (from 30 to 100 pN),[66−68] and FCC SLs formed due to the thermodynamical stability.

For comparison, we conducted a control assembly experiment using the same TTQD NCs but under a different assembly condition: a polar solvent (i.e., ethanol) induced destabilization method (see Experimental Details in Supporting Information).[40,43] In line with the results from the acetone−vapor−exposure and immersion experiments, TTQD SLs formed under this condition exhibited an FCC structure with a lattice constant of 16.1 ± 0.5 nm (Figure S22 and Table S17). In contrast to the cBCC SLs, the resulting FCC SLs retained their initial FCC superstructure after the gentle mashing process (Figure S22, Table S17), indicating an enhanced mechanical stability under external pressure. In general, the mechanical hardness of NC-SL materials can be largely influenced by the packing density of inorganic components.[69] Higher inorganic packing densities typically lead to increased material hardness characterized by higher elastic moduli and greater resistance to deformation when subjected to external forces, and vice versa.[69] However, when assessing the inorganic packing densities of our systems, we observed an intriguing discrepancy: the cBCC SLs, despite their soft nature, exhibit ∼50% higher inorganic packing density than that of the FCC SLs obtained through the solvent-induced destabilization method (Tables S1 and S17). This counterintuitive observation underscores the pivotal role of ligand molecular configurations in imparting the behavior of the SLs in response to the external mechanical forces.[70−72] The ligands in the FCC SLs adopt a straight and rigid configuration as they formed in a polar environment as illustrated in Scheme 2A right,[43,60,73] leading to effective intercalations or partial crystallization among the hydrocarbon chains of the ligands on the surfaces of adjacent NCs (Scheme 2Bii).[60,70,74] As a result, ordered and strong vdW bonds form among the ligands, resulting in stronger interparticle interactions within the FCC SLs hence higher structure stability in response to external mechanical forces.[74,75]

When vaporized solvent molecules approach the cBCC SLs with flexible and coiled ligand configuration (Scheme 2C, step I), the cBCC SL solids start to host the incoming solvent molecules between adjacent TTQD NCs while retaining the initial cBCC superstructure with high structural defect tolerance (Scheme 2C, step a-II and t-II).[76] This solvent molecule inclusion process is supported by the observed SL expansion, as seen in the time-resolved acetone−(or toluene-)vapor−exposure experiment (Figures 3A,B and 4A,B). The initial rapid molecular inclusion and SL expansion observed in stage a1 and t1 are facilitated by solvent molecule diffusion and intake. The subsequent slower molecular inclusion in stage a2 and t2 should be driven by the molecular attraction between the NC surface ligands and the incoming solvent molecules.[36] This interpretation is consistent with the higher solvent molecule inclusion rate and larger resulting unit-cell volume from the toluene-vapor-exposure experiment compared to the acetone−vapor−exposure experiment.

https://doi.org/10.1021/jacs.3c14603
J. Am. Chem. Soc. 2024, 146, 13093−13104

When a solvent such as acetone with intermediate solvent−ligand interfacial energy (2−10 mN/m) is applied in the solvent-vapor-exposure experiment, cBCC SLs can accommodate a limited quantity of solvent molecules. As a result, the initial cBCC superstructure persists for a period of time without undergoing complete dissolution (Figures 2 and 3A). At a microscopic level, the insertion of such solvent molecules into the cBCC NC-SLs increases the polarity of the ligand bilayer microenvironment located between adjacent TTQD NCs. This, in turn, prompts a conformational change in the ligand (i.e., OA or ODPA) from their initial coiled configuration to a straighter arrangement (Scheme 2C, step a-III).[43,60,62−65] Consequently, TTQD NCs start repelling each other, leading to the observed superstructural degradation through inhomogeneous structural distortion and local strain generation, as demonstrated in stage a3. As the distortion level reaches a certain threshold, the initial hierarchical cBCC SL structure undergoes corruption (stage a4) and gradually transforms into the thermodynamically favored FCC SLs through TTQD reorganization (stage a5, Scheme 2C, step a-IV). In contrast, in the toluene-vapor-exposure experiment, a much larger number of solvent molecules can be accommodated by the cBCC NC-SLs. As a result, the superstructure progressively degrades through a supersaturation-triggered spinodal decomposition process followed by full NC dissolution, as shown in stage t3−t5 (Figure 4A−Scheme 2C, Step t-III). Although the result of NC dissolution may seem expected when only considering the initial and final stages, our in situ study of the cBCC NC-SL dissolution process revealed several significant phenomena. These included a substantial SL volume expansion of up to 37.1%, followed by a gradual SL corruption. During this process, the emergence of a spinodal decomposition pattern and the selective detachment of TTQD-dimers occurred subsequently. These findings represent insightful phenomena that we find both exciting and unexpected. They would be otherwise impossible to observe through common ex situ measurements and contribute to a deeper understanding of the dissolution process of NC assemblies in general.

4. CONCLUSIONS

To conclude, we presented a comprehensive investigation into the dynamic behavior of transformable NC-SLs composed of TTQD NCs upon exposure to different solvent molecules. Our mechanistic study based on in situ SAXS measurements revealed that the superstructural transformation was proceeded stepwise, driven by interactions between the incoming molecules and the ligands of the TTQD NC building blocks within the cBCC NC-SLs. Significantly, our study underscores a crucial revelation: seemingly minor and often overlooked elements, such as the fine molecular alignment and configuration of NC surfactant molecules and of guest solvent molecules, can influence inter-NC interactions during and after NC-SL formation. This, in turn, dictates the mechanical characteristics of the resulting NC-SL solids. The results of our investigation provide valuable insights into the interplay among solvent−ligand interactions, molecular recognition, and the formation and transformations of superstructures within dynamic 3D nanoarchitectures. These findings open up a promising avenue for the design and fabrication of innovative materials with tailored functionalities for applications spanning diverse fields, including biomimetics, flexible electronics, and soft robotics.

5. EXPERIMENTAL SECTION

5.1. Chemicals. Acetone, methanol, ethanol, hexanes, chloroform, isopropanol, ethyl acetate, EG, DEG, dimethyl sulfoxide (DMSO), cadmium oxide (CdO, 99.998%), 1-octadecene (ODE, 90%), trioctylphosphine oxide (TOPO 99%), trioctylphosphine (TOP, 97%), oleylamine (OAm, 70%), and 1-octanethiol (>98.5%) were obtained from Sigma-Aldrich. Selenium powder (99.999%) and OA (90%) were purchased from Alfa Aesar. Octadecylphosphonic acid (ODPA, 99%) was purchased from PCI Synthesis.

5.2. Synthesis of TTQDs and cBCC NC-SLs. The cBCC NC-SLs were prepared according to published protocols.[40,41] The building blocks, i.e., TTQDs, were synthesized using a CdSe−CdS core−shell growth protocol. Briefly, 100 nmol of CdSe cores were purified once by washing with methanol. The CdSe core nanocrystals were loaded into a 100 mL three-neck flask with a solvent mixture of 2 mL of ODE and 2 mL of OAm. The reaction mixture was degassed under vacuum at room temperature for 1 h and subsequently at 120 °C for 10 min to remove hexane, water, and oxygen. The reaction mixture was then heated to 310 °C under nitrogen for shell growth. When the temperature reached 240 °C, shell precursor solutions of Cd-oleate (4-monolayer equivalent of CdS shell) and 1-octanethiol (1.2 equiv of Cd-oleate), each dissolved in 2 mL of ODE, were simultaneously added dropwise using a syringe pump at an injection rate of 2 mL/h. 1 hour after the injection was complete, the reaction was stopped by removing the heating mantle and cooling to room temperature by blowing the outside of the flask with cool air. The product was purified by three rounds of precipitation and redispersion using acetone/methanol and hexane. The product was suspended in hexane with a concentration of 20 mg/mL. 2 ml of the TTQD hexane solution was placed in a 20 ml glass vial with a loosely tightened cap to promote slow evaporation, which typically completed in 2 weeks. Faceted precipitations of cBCC NC-SLs were produced, which were subjected to further characterizations and experiments.

5.3. Solvent Immersion Experiment. Solvent immersion experiments were conducted by using cBCC NC-SL powder samples. The sample was loaded on an open diamond anvil with a gasket. A desired solvent was continuously dropped onto the sample for an intended time at room temperature. After immersion, the solvent was quickly drained, and the sample was subjected to additional analysis.

5.4. Vapor Exposure Experiment. Approximately 1.5 mg of the powder form of cBCC NC-SLs was stabilized in a vapor chamber window. The majority of crystallites were below 20 μm in size, ensuring quasi-powder form for SAXS, where random orientational order exists. A vial filled with acetone or toluene was placed in the sample chamber, and synchrotron-based SAXS and WAXS measurements were swiftly initiated after the sample chamber. The Synchrotron X-ray beam had a typical beam size of 200 μm square. X-ray beam irradiation was carried out for 1 s to collect SAXS signals at consistent time intervals. The incident beam intensity remained stable during the in situ measurements. Solvent vapor experiments were performed using a vapor chamber, as shown in Scheme S1 in Supporting Information and Scheme 1 in the main content.

5.5. Mashing Experiment. NC-SLs were mashed by gentle pokes using a needle. The gentle mashing process changed the morphology of cBCC NC-SLs from defined solid powders to an undefined paste-like morphology. SAXS patterns before and after the mashing process were collected to observe the superstructure change.

5.6. Destabilizing Method to Produce NC-SLs under Polar Solvent Conditions. 2 mL of a TTQD NC hexane solution was placed in a 5 mL glass vial, and subsequently, 2 mL of ethanol was slowly added, producing two separated layers of a nonpolar phase containing NCs and a polar phase. The two layers were slowly merged together over several hours. Upon polar solvent (ethanol) diffusing into nonpolar phase (hexane), which contained TTQD NCs, the NCs in solution were destabilized owing to the polarity increase, facilitating NC-SLs formation under a polar solvent condition. The NC-SL samples were generated as precipitation on the inside wall and at the bottom of the vial, which were collected and subjected to further characterizations.

https://doi.org/10.1021/jacs.3c14603
J. Am. Chem. Soc. 2024, 146, 13093−13104

5.7. Synchrotron-Based SAXS and WAXS. We conducted transmission SAXS measurements at the B1 station of the Cornell High Energy Synchrotron Source (CHESS), Cornell University, and the complex materials scattering beamline at NSLS II, Brookhaven National Lab (BNL). At CHESS, using a double circular pinhole aligned tube, monochromatic X-rays at a collimated energy of 25.514 keV were reduced to a small beam with a diameter of 100 μm. SAXS images were collected by using a large area Mar345 detector. At BNL, the X-ray beam (energy of 13.5 keV and beam size of 0.2 × 0.2 mm) was irradiated to the sample, and the scattering signal was collected by a Pilatus 2 M detector. CeO_2 powders were used to calibrate the sample-to-detector distances and associated detector seating parameters. One-dimensional (1D) SAXS plots (i.e., q vs signal) were generated by circularly integrating the two-dimensional (2D) SAXS patterns from the beam center.

5.8. Electron Microscopies. TEM measurements were performed on a JEOL-2100F instrument operated at 200 kV. SEM measurements were performed on a LEO 1530 operated at 3−20 kV.

5.9. SAXS Pattern Analysis. SAXS data analyses were conducted according to the previously reported methods.[77−80] A Multi-Peak Fitting 2.0 package in Igor Pro64 version 9 (WaveMetrics) was used for the SAXS peak analyses. Computer models in this manuscript were created using Autodesk 3dsMax (https://www.autodesk.com/). Python algorithm was applied for peak picking for entire SAXS measurements from the in situ experiments and for simulation of SAXS pattern derived from form factors.

■ ASSOCIATED CONTENT

Supporting Information

The Supporting Information is available free of charge at https://pubs.acs.org/doi/10.1021/jacs.3c14603.

Additional experimental, computer model study, calculation including SAXS simulation, photographs, and TEM images (PDF)

In situ 2D SAXS results from the acetone−vapor−exposure experiment (a vapor pressure of 30.8 KPa) (Movie S1) (MP4)

In situ 1D SAXS results from the acetone−vapor−exposure experiment (Movie S2) (MP4)

In situ 2D SAXS results from the toluene−vapor−exposure experiment (a vapor pressure of 3.76 KPa) (Movie S3) (MP4)

In situ 1D SAXS results from the toluene−vapor−exposure experiment (Movie S4) (MP4)

■ AUTHOR INFORMATION

Corresponding Author

Ou Chen − *Department of Chemistry, Brown University, Providence, Rhode Island 02912, United States;* orcid.org/0000-0003-0551-090X; Email: ouchen@brown.edu

Authors

Yasutaka Nagaoka − *Department of Chemistry, Brown University, Providence, Rhode Island 02912, United States;* orcid.org/0000-0001-8612-2612

Jeremy Schneider − *Department of Chemistry, Brown University, Providence, Rhode Island 02912, United States;* orcid.org/0000-0002-2026-7533

Na Jin − *Department of Chemistry, Brown University, Providence, Rhode Island 02912, United States*

Tong Cai − *Department of Chemistry, Brown University, Providence, Rhode Island 02912, United States*

Yuzi Liu − *Center for Nanoscale Materials, Argonne National Laboratory, Argonne, Illinois 60439, United States;* orcid.org/0000-0002-8733-1683

Zhongwu Wang − *Cornell High Energy Synchrotron Source, Cornell University, Ithaca, New York 14853, United States;* orcid.org/0000-0001-9742-5213

Ruipeng Li − *National Synchrotron Light Source II, Brookhaven National Laboratory, Upton, New York 11973, United States*

Kyung-Suk Kim − *School of Engineering, Brown University, Providence, Rhode Island 02912, United States*

Complete contact information is available at: https://pubs.acs.org/10.1021/jacs.3c14603

Funding

O.C. thanks the National Science Foundation, under Award No. DMR-1943930, for their support. O. C. and K.S.K. thank the National Science Foundation, under Award No. CMMI-1934314, for their support. O.C. also acknowledges the support from the Alfred P. Sloan Foundation through the Sloan Research Fellowship Award program, and the 3 M Foundation through the Non-Tenured Faculty Award program. This research used the CMS beamline of the National Synchrotron Light Source II, a U.S. Department of Energy (DOE), Office of Science User Facility, operated for the DOE, Office of Science, by the Brookhaven National Laboratory under Contract DE-SC0012704. The electron microscopy research conducted at the Argonne National Laboratory, Center for Nanoscale Materials, U.S. Department of Energy Office of Science User Facility, was supported by the U.S. DOE, Office of Basic Energy Sciences, under Contract No. DE-AC02-06CH11357. CHESS was supported by the NSF awards DMR-1332208 and DMR-1829070.

Notes

The authors declare no competing financial interest.

■ ACKNOWLEDGMENTS

O.C. acknowledges support for TEM and XRD measurements performed at the Institute for Molecular and Nanoscale Innovation (IMNI) at Brown University.

■ REFERENCES

(1) Yang, Y.; Jiao, P. C. Nanomaterials and Nanotechnology for Biomedical Soft Robots. *Mater. Today Adv.* **2023**, *17*, 100338.

(2) Sarikaya, M.; Tamerler, C.; Jen, A. K. Y.; Schulten, K.; Baneyx, F. Molecular Biomimetics: Nanotechnology through Biology. *Nat. Mater.* **2003**, *2* (9), 577−585.

(3) Grzybowski, B. A.; Fitzner, K.; Paczesny, J.; Granick, S. From Dynamic Self-Assembly to Networked Chemical Systems. *Chem. Soc. Rev.* **2017**, *46* (18), 5647−5678.

(4) Li, J. X.; de Ávila, B. E. F.; Gao, W.; Zhang, L. F.; Wang, J. Micro/Nanorobots for Biomedicine: Delivery, Surgery, Sensing, and Detoxification. *Sci. Robot.* **2017**, *2* (4), No. eaam6431.

(5) Matsuhisa, N.; Niu, S. M.; O'Neill, S. J. K.; Kang, J. H.; Ochiai, Y.; Katsumata, T.; Wu, H. C.; Ashizawa, M.; Wang, G. J. N.; Zhong, D. L.; et al. High-Frequency and Intrinsically Stretchable Polymer Diodes. *Nature* **2021**, *600* (7888), 246−252.

(6) Sun, Y. G.; Rogers, J. A. Inorganic Semiconductors for Flexible Electronics. *Adv. Mater.* **2007**, *19* (15), 1897−1916.

(7) Ilievski, F.; Mazzeo, A. D.; Shepherd, R. F.; Chen, X.; Whitesides, G. M. Soft Robotics for Chemists. *Angew. Chem., Int. Ed.* **2011**, *50* (8), 1890−1895.

(8) Bisoyi, H. K.; Li, Q. Liquid Crystals: Versatile Self-Organized Smart Soft Materials. *Chem. Rev.* **2022**, *122* (5), 4887−4926.

(9) Hu, C. Z.; Pane, S.; Nelson, B. J. Soft Micro- and Nanorobotics. *Annu. Rev. Contr. Robot* **2018**, *1*, 53−75.
(10) Majidi, C. Soft Robotics: A Perspective-Current Trends and Prospects for the Future. *Soft Robot* **2014**, *1* (1), 5−11.
(11) Shen, Z. Q.; Chen, F. F.; Zhu, X. Y.; Yong, K. T.; Gu, G. Y. Stimuli-Responsive Functional Materials for Soft Robotics. *J. Mater. Chem. B* **2020**, *8* (39), 8972−8991.
(12) Koshima, H. *Mechanically Responsive Materials for Soft Robotics*; Wiley VCH, 2020.
(13) Ryabchun, A.; Li, Q.; Lancia, F.; Aprahamian, I.; Katsonis, N. Shape-Persistent Actuators from Hydrazone Photoswitches. *J. Am. Chem. Soc.* **2019**, *141* (3), 1196−1200.
(14) Yue, Y. F.; Norikane, Y.; Azumi, R.; Koyama, E. Light-Induced Mechanical Response in Crosslinked Liquid-Crystalline Polymers with Photoswitchable Glass Transition Temperatures. *Nat. Commun.* **2018**, *9*, 3234.
(15) Ikeda, T.; Tsutsumi, O. Optical Switching and Image Storage by Means of Azobenzene Liquid-Crystal Films. *Science* **1995**, *268* (5219), 1873−1875.
(16) Kuzina, M. A.; Kartsev, D. D.; Stratonovich, A. V.; Levkin, P. A. Organogels versus Hydrogels: Advantages, Challenges, and Applications. *Adv. Funct. Mater.* **2023**, *33* (27), 202301421.
(17) Guo, S. F.; Matsukawa, K.; Miyata, T.; Okubo, T.; Kuroda, K.; Shimojima, A. Photoinduced Bending of Self-Assembled Azobenzene Siloxane Hybrid. *J. Am. Chem. Soc.* **2015**, *137* (49), 15434−15440.
(18) Mattia, E.; Otto, S. Supramolecular Systems Chemistry. *Nat. Nanotechnol.* **2015**, *10* (2), 111−119.
(19) Gu, P. Y.; Luo, X. B.; Zhou, S. Y.; Wang, D. F.; Li, Z. Y.; Chai, Y.; Zhang, Y. Z.; Shi, S. W.; Russell, T. P. Stabilizing Liquids Using Interfacial Supramolecular Assemblies. *Angew. Chem. Int. Ed.* **2023**, *62*, No. e202303789.
(20) Israelachvili, J. N. *Intermolecular and Surface Forces*, 3 ed.; Academic Press, 2011.
(21) Bishop, K. J. M.; Wilmer, C. E.; Soh, S.; Grzybowski, B. A. Nanoscale Forces and Their Uses in Self-Assembly. *Small* **2009**, *5* (14), 1600−1630.
(22) Zhao, X. H.; Chen, X. Y.; Yuk, H.; Lin, S. T.; Liu, X. Y.; Parada, G. Soft Materials by Design: Unconventional Polymer Networks Give Extreme Properties. *Chem. Rev.* **2021**, *121* (8), 4309−4372.
(23) Dong, J. Q.; Davis, A. P. Molecular Recognition Mediated by Hydrogen Bonding in Aqueous Media. *Angew. Chem. Int. Ed.* **2021**, *60* (15), 8035−8048.
(24) Yee, D. W.; Lee, M. S.; An, J. Y.; Macfarlane, R. J. Reversible Diffusionless Phase Transitions in 3D Nanoparticle Superlattices. *J. Am. Chem. Soc.* **2023**, *145* (11), 6051−6056.
(25) Williamson, C. B.; Nevers, D. R.; Nelson, A.; Hadar, I.; Banin, U.; Hanrath, T.; Robinson, R. D. Chemically Reversible Isomerization of Inorganic Clusters. *Science* **2019**, *363* (6428), 731−735.
(26) Pal, S.; Zhang, Y. G.; Kumar, S. K.; Gang, O. Dynamic Tuning of DNA-Nanoparticle Superlattices by Molecular Intercalation of Double Helix. *J. Am. Chem. Soc.* **2015**, *137* (12), 4030−4033.
(27) Li, Z.; Fan, Q.; Ye, Z.; Wu, C.; Wang, Z.; Yin, Y. A Magnetic Assembly Approach to Chiral Superstructures. *Science* **2023**, *380* (6652), 1384−1390.
(28) Cherniukh, I.; Rainò, G.; Stöferle, T.; Burian, M.; Travesset, A.; Naumenko, D.; Amenitsch, H.; Erni, R.; Mahrt, R. F.; Bodnarchuk, M. I.; et al. Perovskite-Type Superlattices from Lead Halide Perovskite Nanocubes. *Nature* **2021**, *593* (7860), 535−542.
(29) Marino, E.; LaCour, R. A.; Moore, T. C.; van Dongen, S. W.; Keller, A. W.; An, D.; Yang, S.; Rosen, D. J.; Gouget, G.; Tsai, E. H. R.; et al. Crystallization of Binary Nanocrystal Superlattices and the Relevance of Short-Range Attraction. *Nat. Synth.* **2023**, *3*, 111−122.
(30) Mueller, N. S.; Okamura, Y.; Vieira, B. G. M.; Juergensen, S.; Lange, H.; Barros, E. B.; Schulz, F.; Reich, S. Deep Strong Light-Matter Coupling in Plasmonic Nanoparticle Crystals. *Nature* **2020**, *583* (7818), 780−784.
(31) Deng, K. R.; Luo, Z. S.; Tan, L.; Quan, Z. W. Self-Assembly of Anisotropic Nanoparticles into Functional Superstructures. *Chem. Soc. Rev.* **2020**, *49* (16), 6002−6038.
(32) Tan, R.; Zhu, H.; Cao, C.; Chen, O. Multi-Component Superstructures Self-Assembled from Nanocrystal Building Blocks. *Nanoscale* **2016**, *8* (19), 9944−9961.
(33) Zhu, H.; Fan, Z. C.; Song, S. Y.; Eggert, D.; Liu, Y. Z.; Shi, W. W.; Yuan, Y. C.; Kim, K. S.; Grünwald, M.; Chen, O. Dual Atomic Coherence in the Self-Assembly of Patchy Heterostructural Nanocrystals. *ACS Nano* **2022**, *16* (9), 15053−15062.
(34) Boles, M. A.; Engel, M.; Talapin, D. V. Self-Assembly of Colloidal Nanocrystals: From Intricate Structures to Functional Materials. *Chem. Rev.* **2016**, *116* (18), 11220−11289.
(35) Wei, W. B.; Bai, F.; Fan, H. Y. Surfactant-Assisted Cooperative Self-Assembly of Nanoparticles into Active Nanostructures. *iScience* **2019**, *11*, 272−293.
(36) Nagaoka, Y.; Chen, O.; Wang, Z. W.; Cao, Y. C. Structural Control of Nanocrystal Superlattices Using Organic Guest Molecules. *J. Am. Chem. Soc.* **2012**, *134* (6), 2868−2871.
(37) Weidman, M. C.; Smilgies, D. M.; Tisdale, W. A. Kinetics of the Self-Assembly of Nanocrystal Superlattices Measured by Real-Time In Situ X-ray Scattering. *Nat. Mater.* **2016**, *15* (7), 775−781.
(38) Zhou, S.; Li, J. H.; Lu, J.; Liu, H. H.; Kim, J. Y.; Kim, A.; Yao, L. H.; Liu, C.; Qian, C.; Hood, Z. D.; et al. Chiral Assemblies of Pinwheel Superlattices on Substrates. *Nature* **2022**, *612* (7939), 259−265.
(39) Geuchies, J. J.; van Overbeek, C.; Evers, W. H.; Goris, B.; de Backer, A.; Gantapara, A. P.; Rabouw, F. T.; Hilhorst, J.; Peters, J. L.; Konovalov, O.; et al. In Situ Study of the Formation Mechanism of Two-Dimensional Superlattices from PbSe Nanocrystals. *Nat. Mater.* **2016**, *15* (12), 1248−1254.
(40) Nagaoka, Y.; Tan, R.; Li, R. P.; Zhu, H.; Eggert, D.; Wu, Y. A.; Liu, Y. Z.; Wang, Z. W.; Chen, O. Superstructures Generated from Truncated Tetrahedral Quantum Dots. *Nature* **2018**, *561* (7723), 378−382.
(41) Tan, R.; Yuan, Y. C.; Nagaoka, Y.; Eggert, D.; Wang, X. D.; Thota, S.; Guo, P.; Yang, H. R.; Zhao, J.; Chen, O. Monodisperse Hexagonal Pyramidal and Bipyramidal Wurtzite CdSe-CdS Core-Shell Nanocrystals. *Chem. Mater.* **2017**, *29* (9), 4097−4108.
(42) Nagaoka, Y.; Zhu, H.; Eggert, D.; Chen, O. Single-Component Quasicrystalline Nanocrystal Superlattices through Flexible Polygon Tiling Rule. *Science* **2018**, *362* (6421), 1396−1400.
(43) Boles, M. A.; Talapin, D. V. Self-Assembly of Tetrahedral CdSe Nanocrystals: Effective "Patchiness" via Anisotropic Steric Interaction. *J. Am. Chem. Soc.* **2014**, *136* (16), 5868−5871.
(44) Speriosu, V. S. Kinematical X-Ray-Diffraction in Nonuniform Crystalline Films - Strain and Damage Distributions in Ion-Implanted Garnets. *J. Appl. Phys.* **1981**, *52* (10), 6094−6103.
(45) Loh, N. D.; Sen, S.; Bosman, M.; Tan, S. F.; Zhong, J.; Nijhuis, C. A.; Kral, P.; Matsudaira, P.; Mirsaidov, U. Multistep Nucleation of Nanocrystals in Aqueous Solution. *Nat. Chem.* **2017**, *9* (1), 77−82.
(46) Cahn, J. W. On Spinodal Decomposition. *Acta Metall. Mater.* **1961**, *9* (9), 795−801.
(47) Li, L.; Miesch, C.; Sudeep, P. K.; Balazs, A. C.; Emrick, T.; Russell, T. P.; Hayward, R. C. Kinetically Trapped Co-continuous Polymer Morphologies through Intraphase Gelation of Nanoparticles. *Nano Lett.* **2011**, *11* (5), 1997−2003.
(48) Takagishi, H.; Masuda, T.; Shimoda, T.; Maezono, R.; Hongo, K. Method for the Calculation of the Hamaker Constants of Organic Materials by the Lifshitz Macroscopic Approach with Density Functional Theory. *J. Phys. Chem. A* **2019**, *123* (40), 8726−8733.
(49) Abbott, S. *Hansen Solubility Parameters*. https://www.hansen-solubility.com/(accessed Dec 15, 2023).
(50) Adamson, A. W.; Gast, A. P. *Physical Chemistry of Surfaces*; Wiley, 1997.
(51) Bai, F.; Bian, K. F.; Huang, X.; Wang, Z. W.; Fan, H. Y. Pressure Induced Nanoparticle Phase Behavior, Property, and Applications. *Chem. Rev.* **2019**, *119* (12), 7673−7717.
(52) Nagaoka, Y.; Hills-Kimball, K.; Tan, R.; Li, R. P.; Wang, Z. W.; Chen, O. Nanocube Superlattices of Cesium Lead Bromide Perovskites and Pressure-Induced Phase Transformations at Atomic and Mesoscale Levels. *Adv. Mater.* **2017**, *29* (18), 1606666.

https://doi.org/10.1021/jacs.3c14603
J. Am. Chem. Soc. 2024, 146, 13093−13104

(53) Zhu, H.; Nagaoka, Y.; Hills-Kimball, K.; Tan, R.; Yu, L.; Fang, Y.; Wang, K.; Li, R. P.; Wang, Z. W.; Chen, O. Pressure-Enabled Synthesis of Hetero-Dimers and Hetero-Rods through Intraparticle Coalescence and Interparticle Fusion of Quantum-Dot-Au Satellite Nanocrystals. *J. Am. Chem. Soc.* **2017**, *139* (25), 8408−8411.
(54) Xiao, T. Y.; Nagaoka, Y.; Wang, X. R.; Jiang, T.; LaMontagne, D.; Zhang, Q.; Cao, C.; Diao, X. Z.; Qiu, J. H.; Lu, Y. R.; et al. Nanocrystals with Metastable High-Pressure Phases under Ambient Conditions. *Science* **2022**, *377* (6608), 870−874.
(55) Nagaoka, Y.; Saghy, P.; Chen, O. The Art of Peer Pressure between Nanocrystals: High-Pressure Surface Nanochemistry. *MRS Commun.* **2023**, *13*, 928−941.
(56) Li, Q.; Xu, B.; Chen, Z. W.; Han, J.; Tan, L.; Luo, Z. S.; Shen, P. F.; Quan, Z. W. Excitation-Dependent Emission Color Tuning of 0D Cs_2InBr_5• H_2O at High Pressure. *Adv. Funct. Mater.* **2021**, *31* (38), 2104923.
(57) Zhang, L.; Li, S. X.; Sun, H. Y.; Jiang, Q. W.; Wang, Y.; Fang, Y. Y.; Shi, Y.; Duan, D. F.; Wang, K.; Jiang, H.; et al. Revealing the Mechanism of Pressure-Induced Emission in Layered Silver-Bismuth Double Perovskites. *Angew. Chem., Int. Ed.* **2023**, *62*, No. e202301573.
(58) Elbert, K. C.; Jishkariani, D.; Wu, Y. T.; Lee, J. D.; Donnio, B.; Murray, C. B. Design, Self-Assembly, and Switchable Wettability in Hydrophobic, Hydrophilic, and Janus Dendritic Ligand-Gold Nanoparticle Hybrid Materials. *Chem. Mater.* **2017**, *29* (20), 8737−8746.
(59) Zhang, Z. Y.; Wang, W. L.; Korpacz, A. N.; Dufour, C. R.; Weiland, Z. J.; Lambert, C. R.; Timko, M. T. Binary Liquid Mixture Contact-Angle Measurements for Precise Estimation of Surface Free Energy. *Langmuir* **2019**, *35* (38), 12317−12325.
(60) Monego, D.; Kister, T.; Kirkwood, N.; Doblas, D.; Mulvaney, P.; Kraus, T.; Widmer-Cooper, A. When Like Destabilizes Like: Inverted Solvent Effects in Apolar Nanoparticle Dispersions. *ACS Nano* **2020**, *14* (5), 5278−5287.
(61) Talapin, D. V.; Shevchenko, E. V.; Bodnarchuk, M. I.; Ye, X. C.; Chen, J.; Murray, C. B. Quasicrystalline Order in Self-Assembled Binary Nanoparticle Superlattices. *Nature* **2009**, *461* (7266), 964−967.
(62) Cordeiro, M. A. L.; Leite, E. R.; Stach, E. A. Controlling the Formation and Structure of Nanoparticle Superlattices through Surface Ligand Behavior. *Langmuir* **2016**, *32* (44), 11606−11614.
(63) De Roo, J.; Yazdani, N.; Drijvers, E.; Lauria, A.; Maes, J.; Owen, J. S.; Van Driessche, I.; Niederberger, M.; Wood, V.; Martins, J. C.; et al. Probing Solvent-Ligand Interactions in Colloidal Nanocrystals by the NMR Line Broadening. *Chem. Mater.* **2018**, *30* (15), 5485−5492.
(64) Goubet, N.; Richardi, J.; Albouy, P. A.; Pileni, M. P. Which Forces Control Supracrystal Nucleation in Organic Media? *Adv. Funct. Mater.* **2011**, *21* (14), 2693−2704.
(65) Hummer, G.; Garde, S.; Garcia, A. E.; Pohorille, A.; Pratt, L. R. An Information Theory Model of Hydrophobic Interactions. *Proc. Natl. Acad. Sci. U.S.A.* **1996**, *93* (17), 8951−8955.
(66) Kramb, R. C.; Zukoski, C. F. A Metastable van der Waals Gel: Transitioning from Weak to Strong Attractions. *Langmuir* **2008**, *24* (14), 7565−7572.
(67) Zang, Y. P.; Zhang, F. J.; Di, C. A.; Zhu, D. B. Advances of Flexible Pressure Sensors toward Artificial Intelligence and Health Care Applications. *Mater. Horiz.* **2015**, *2* (2), 140−156.
(68) Wenzler, L. A.; Moyes, G. L.; Olson, L. G.; Harris, J. M.; Beebe, T. P. Single Molecule Bond-Rupture Force Analysis of Interactions between AFM Tips and Substrates Modified with Organosilanes. *Anal. Chem.* **1997**, *69* (14), 2855−2861.
(69) Dowling, N. E. *Mechanical Behavior of Materials*; Pearson Education, 2011.
(70) Dreyer, A.; Feld, A.; Kornowski, A.; Yilmaz, E. D.; Noei, H.; Meyer, A.; Krekeler, T.; Jiao, C. G.; Stierle, A.; Abetz, V.; et al. Organically Linked Iron Oxide Nanoparticle Supercrystals with Exceptional Isotropic Mechanical Properties. *Nat. Mater.* **2016**, *15* (5), 522−528.
(71) Nagaoka, Y.; Suda, M.; Yoon, I.; Chen, N.; Yang, H. J.; Liu, Y. Z.; Anzures, B. A.; Parman, S. W.; Wang, Z. W.; Grünwald, M.; et al. Bulk Grain-Boundary Materials from Nanocrystals. *Chem.* **2021**, *7* (2), 509−525.
(72) Podsiadlo, P.; Krylova, G.; Lee, B.; Critchley, K.; Gosztola, D. J.; Talapin, D. V.; Ashby, P. D.; Shevchenko, E. V. The Role of Order, Nanocrystal Size, and Capping Ligands in the Collective Mechanical Response of Three-Dimensional Nanocrystal Solids. *J. Am. Chem. Soc.* **2010**, *132* (26), 8953−8960.
(73) Kister, T.; Monego, D.; Mulvaney, P.; Widmer-Cooper, A.; Kraus, T. Colloidal Stability of Apolar Nanoparticles: The Role of Particle Size and Ligand Shell Structure. *ACS Nano* **2018**, *12* (6), 5969−5977.
(74) Plunkett, A.; Kampferbeck, M.; Bor, B.; Sazama, U.; Krekeler, T.; Bekaert, L.; Noei, H.; Giuntini, D.; Fröba, M.; Stierle, A.; et al. Strengthening Engineered Nanocrystal Three-Dimensional Superlattices via Ligand Conformation and Reactivity. *ACS Nano* **2022**, *16* (8), 11692−11707.
(75) Yang, L. X.; Adam, C.; Nichol, G. S.; Cockroft, S. L. How Much Do van der Waals Dispersion Forces Contribute to Molecular Recognition in Solution? *Nat. Chem.* **2013**, *5* (12), 1006−1010.
(76) Binder, W. H. The "labile" Chemical Bond: A Perspective on Mechanochemistry in Polymers. *Polymer* **2020**, *202*, 122639.
(77) Förster, S.; Timmann, A.; Konrad, M.; Schellbach, C.; Meyer, A.; Funari, S. S.; Mulvaney, P.; Knott, R. Scattering Curves of Ordered Mesoscopic Materials. *J. Phys. Chem. B* **2005**, *109* (4), 1347−1360.
(78) Förster, S.; Timmann, A.; Schellbach, C.; Frömsdorf, A.; Kornowski, A.; Weller, H.; Roth, S. V.; Lindner, P. Order Causes Secondary Bragg Peaks in Soft Materials. *Nat. Mater.* **2007**, *6*, 888−893.
(79) Marino, E.; Rosen, D. J.; Yang, S.; Tsai, E. H.; Murray, C. B. Temperature-Controlled Reversible Formation and Phase Transformation of 3D Nanocrystal Superlattices Through In Situ Small-Angle X-ray Scattering. *Nano Lett.* **2023**, *23* (10), 4250−4257.
(80) Lokteva, I.; Dartsch, M.; Dallari, F.; Westermeier, F.; Walther, M.; Grübel, G.; Lehmkühler, F. Real-Time X-ray Scattering Discovers Rich Phase Behavior in PbS Nanocrystal Superlattices during In Situ Assembly. *Chem. Mater.* **2021**, *33* (16), 6553−6563.

https://doi.org/10.1021/jacs.3c14603
J. Am. Chem. Soc. 2024, 146, 13093−13104